

Knockdown of NADPH oxidase 4 reduces mitochondrial oxidative stress and neuronal pyroptosis following intracerebral hemorrhage

Bo-Yun Ding^{1, #}, Chang-Nan Xie^{2, #}, Jia-Yu Xie¹, Zhuo-Wei Gao³, Xiao-Wei Fei⁴, En-Hui Hong¹, Wen-Jin Chen⁵, Yi-Zhao Chen^{1, 6, *}

<https://doi.org/10.4103/1673-5374.360249>

Date of submission: May 11, 2022

Date of decision: June 20, 2022

Date of acceptance: September 16, 2022

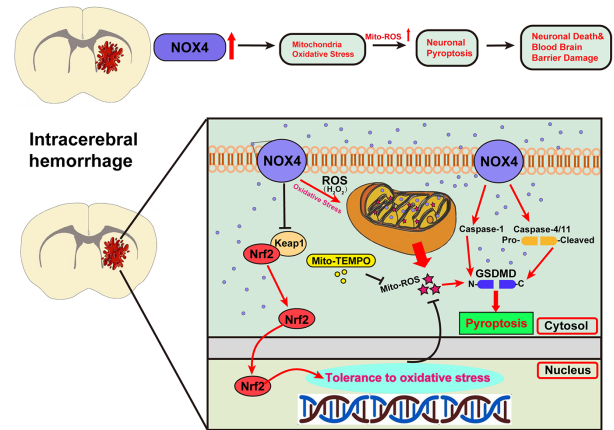
Date of web publication: November 9, 2022

From the Contents

Introduction	1734
Methods	1735
Results	1736
Discussion	1740

Graphical Abstract

Increased NOX4 expression after intracerebral hemorrhage causes neuronal pyroptosis and mitochondrial oxidative stress and damages the blood-brain barrier, resulting in secondary brain injury



Abstract

Intracerebral hemorrhage is often accompanied by oxidative stress induced by reactive oxygen species, which causes abnormal mitochondrial function and secondary reactive oxygen species generation. This creates a vicious cycle leading to reactive oxygen species accumulation, resulting in progression of the pathological process. Therefore, breaking the cycle to inhibit reactive oxygen species accumulation is critical for reducing neuronal death after intracerebral hemorrhage. Our previous study found that increased expression of nicotinamide adenine dinucleotide phosphate oxidase 4 (NADPH oxidase 4, NOX4) led to neuronal apoptosis and damage to the blood-brain barrier after intracerebral hemorrhage. The purpose of this study was to investigate the role of NOX4 in the circle involving the neuronal tolerance to oxidative stress, mitochondrial reactive oxygen species and modes of neuronal death other than apoptosis after intracerebral hemorrhage. We found that NOX4 knockdown by adeno-associated virus (AAV-NOX4) in rats enhanced neuronal tolerance to oxidative stress, enabling them to better resist the oxidative stress caused by intracerebral hemorrhage. Knockdown of NOX4 also reduced the production of reactive oxygen species in the mitochondria, relieved mitochondrial damage, prevented secondary reactive oxygen species accumulation, reduced neuronal pyroptosis and contributed to relieving secondary brain injury after intracerebral hemorrhage in rats. Finally, we used a mitochondria-targeted superoxide dismutase mimetic to explore the relationship between reactive oxygen species and NOX4. The mitochondria-targeted superoxide dismutase mimetic inhibited the expression of NOX4 and neuronal pyroptosis, which is similar to the effect of AAV-NOX4. This indicates that NOX4 is likely to be an important target for inhibiting mitochondrial reactive oxygen species production, and NOX4 inhibitors can be used to alleviate oxidative stress response induced by intracerebral hemorrhage.

Key Words: caspase 1; caspase4/11; gasdermin D; intracerebral hemorrhage; mitochondria reactive oxygen species inhibitor; NADPH oxidase 4; neuronal pyroptosis; neuronal tolerance; reactive oxygen species; secondary brain injury

Introduction

Intracerebral hemorrhage (ICH) is associated with high mortality and disability rates and accounts for approximately 10–15% of stroke cases worldwide (Wu et al., 2022). Presently, there is no effective treatment for ICH, and the efficacy of commonly used clinical treatment methods, such as hematoma clearance, is not satisfactory (Hu et al., 2016). Previous studies have shown that brain damage caused by ICH is not only related to the hematoma itself, but also to oxidative stress in the adjacent tissues (Feng et al., 2015; Jin et al., 2022). Therefore, there is an urgent need to explore strategies to inhibit oxidative stress to treat ICH.

Several studies have shown that the production of reactive oxygen species

(ROS) is increased after ICH, leading to oxidative stress and ultimately to cellular oxidative damage (Ding et al., 2014; Zhu et al., 2021). Nicotinamide adenine dinucleotide phosphate oxidase (NOX) is the only enzyme whose primary function is known to generate ROS (Brown and Borutaite, 2012; Haslund-Vinding et al., 2017). The ROS produced by NOX causes mitochondrial dysfunction, producing secondary ROS, which, together with the primary ROS produced by NOX, can cause additional ROS accumulation in tissue, forming a vicious circle of oxidative stress in tissues (Drummond and Sobey, 2014). Breaking this circle, starting with the mitochondria, and inhibiting the accumulation of ROS is critical for reducing neuronal death after ICH.

NOX4 is the only NOX subtype that is activated in tissues without the help of other envelope regulatory subunits (Schürmann et al., 2015). Its main product

¹Guangdong Provincial Key Laboratory on Brain Function Repair and Regeneration, Department of Neurosurgery, Zhujiang Hospital, The National Key Clinical Specialty, The Neurosurgery Institute of Guangdong Province, The Engineering Technology Research Center of Education Ministry of China, Southern Medical University, Guangzhou, Guangdong Province, China; ²Department of Spinal Surgery, Orthopedic Medical Center, Zhujiang Hospital, Southern Medical University, Guangzhou, Guangdong Province, China; ³Department of Traditional Chinese Medicine, The Third Affiliated Hospital of Southern Medical University, Guangzhou, Guangdong Province, China; ⁴Department of Neurosurgery, Xijing Hospital, Air Force Military Medical University, Xi'an, Shaanxi Province, China; ⁵Department of Neurosurgery, Peking University Shenzhen Hospital, Shenzhen Peking University-The Hong Kong University of Science and Technology Medical Center, Shenzhen, Guangdong Province, China; ⁶Department of Neurosurgery, The First Affiliated Hospital of Guangzhou Medical University, Guangzhou Medical University, Guangzhou, Guangdong Province, China

*Correspondence to: Yi-Zhao Chen, PhD, chenyzhaophd@163.com.

<https://orcid.org/0000-0003-4765-5699> (Bo-Yun Ding); <https://orcid.org/0000-0002-7357-9127> (Yi-Zhao Chen)

#Both authors contributed equally to this work.

Funding: This study was supported by the National Natural Science Foundation of China, No. 81671125; the Natural Science Foundation of Guangdong Province, No. 2021A1515011115; and Guangzhou Science and Technology Project, No. 202102010346 (all to YZC).

How to cite this article: Ding BY, Xie CN, Xie JY, Gao ZW, Fei XW, Hong EH, Chen WJ, Chen YZ (2023) Knockdown of NADPH oxidase 4 reduces mitochondrial oxidative stress and neuronal pyroptosis following intracerebral hemorrhage. *Neural Regen Res* 18(8):1734-1742.

is hydrogen peroxide, which has a longer half-life and better tissue activity than superoxide; it is thus easier for hydrogen peroxide to pass through the cell membranes to play an important role in cell signal transduction (Nisimoto et al., 2014). Our previous study found that NOX4 expression was up-regulated following ICH, resulting in neuronal apoptosis and blood-brain barrier (BBB) damage because of secondary brain injury (SBI) (Xie et al., 2020).

Pyroptosis is a form of cell death caused by the activation of various caspases (caspases 1, 3, 4, 5, 7, 8, and 11) mediated by an inflammasome and the shearing/polymerization of various Gasdermin family members (Kayagaki et al., 2011). Pyroptosis is characterized by rapid rupture of the plasma membrane, leading to released cellular contents and cytokines and the formation of plasma membrane pores, which eventually cause water influx, cellular swelling and rupture (Bergsbaken et al., 2009). Similar to apoptosis, during pyroptosis, cleavage of chromosome DNA also occurs but the nucleus remains intact (Bergsbaken and Cookson, 2007). A previous study reported that inhibition of NOX4 reversed cardiomyocyte pyroptosis in dilated cardiomyopathy (Zeng et al., 2020). Whether NOX4 mediates neuronal pyroptosis after ICH is still unknown, which is worth further exploring.

In this study, we investigated the potential role of NOX4 in the production of mitochondrial ROS and neuronal pyroptosis after ICH. We identified the nerve cells in which NOX4 increases and whether NOX4 is involved in ROS production and other neuronal death modes in a rat model for ICH.

Methods

Animals and ethics statement

Adult male Sprague-Dawley rats (8-week-old) weighing 280–320 g were purchased from the Laboratory Animal Center of Southern Medical University (Guangzhou, Guangdong, China; license No. SCXK (Yue) 2020-0051) and housed in the Experimental Animal Center of Zhujiang Hospital (three rats/cage) under a standard 12-hour light/dark cycle and specific-pathogen-free conditions (temperature 18–26°C, humidity 40–70%, noise < 85 dB, ammonia concentration < 20 ppm and ventilation 8–12 times/h), with free access to food and water.

The rats were randomly divided into Sham, ICH, ICH + AAV-CON and ICH + AAV-NOX4 groups ($n = 6/\text{group}$). AAV-NOX4 transfection was performed 14 days before ICH modeling and rat brain was extracted on the third day of modeling for subsequent experiments. The entire experiment lasted about 17 days. In other experiments *in vivo*, the rats were randomly divided into Sham, ICH, ICH + AAV-NOX4 and ICH + Mito-TEMPO groups ($n = 6/\text{group}$). In the ICH + AAV-NOX4 group, AAV-NOX4 transfection was performed 14 days before ICH modeling and mouse brain was extracted on the third day of modeling for subsequent experiments. In the ICH + Mito-TEMPO group, Mito-TEMPO was injected into the brain while modeling. The entire experiments *in vivo* lasted about 17 days. *In vitro* experiment, the cells were randomly divided into Sham, H₂O₂, H₂O₂ + AAV-CON and H₂O₂ + AAV-NOX4 groups ($n = 6/\text{group}$).

All animal experiments conducted in this study were approved by the Animal Ethics Committee of Southern Medical University (approval No. LAEC-2020-123) on August 7, 2020. All experiments were designed and reported according to the Animal Research: Reporting of *In Vivo* Experiments (ARRIVE) guidelines (Percie du Sert et al., 2020).

ICH model

Rats were intraperitoneally injected with 3% sodium pentobarbital (2 mL/kg, Cat# Tc-P8411, Merck, Darmstadt, Germany). Type IV collagenase (0.2 U in 1 μL sterile saline; Thermo Fisher Scientific, Waltham, MA, USA, Cat# 17104019.) was injected into the right basal ganglia using a stereo locator (Cat# 68025, RWD, Shenzhen, China) as previously described (Schlunk et al., 2015). The stereo locator coordinates were as follows: 1.5 mm for the anterior fontanelle, 3.5 mm for the side and 6.0 mm for the depth (Xie et al., 2020). Type IV collagenase (0.4 μL) was slowly injected into the basal ganglia over 30 minutes using a microsyringe (5 μL , High Pigeon Industry, Shanghai, China) with a micro-single push injection pump (Longer, Baoding, China). The needle was held for 3 minutes after injection to prevent backflow. Bone wax was used to seal the pinhole in the skull and close the wound. In the sham group, normal saline (0.4 μL) was injected in the same way as in the ICH group (Xie et al., 2020). The vital signs of the rats were stable during the entire process and anesthesia was maintained. The rats were placed on an electric blanket; after they woke up from the anesthesia, they were returned to their cages where they were given the same food and water as before the modeling.

Adeno-associated virus construction and *in vivo* injection

The adeno-associated virus (AAV) used in this study was constructed as previously reported (Piras et al., 2016). Briefly, AAV9 carrying U6 and green fluorescent protein (GFP) sequences and driving the expression of short hairpin RNA (shRNA) targeting NOX4 or control shRNA were used in this study: AAV9-U6-shRNA(NOX4)-CMV-GFP (AAV-NOX4) and AAV9-U6-shRNA(Scramble)-CMV-GFP (AAV-CON) (Vizin Biologics, Jinan, China). The shRNA sequences used in this study are as follows: shRNA (NOX4): forward: 5'-GCC AAC GAA GGG GTT AAA CA-3', reverse: 5'-CTT CTG TGA TCC GCG AAG GT-3'; shRNA (scramble): 5'-TTC TCC GAA CGT GTC ACG TTT CAA GAG AAG GTG ACA CGT TCG GAG AAT TTT TT-3'.

The shRNA against NOX4 was cloned into Vigenebio shRNA AAV vector, and the recombinant plasmid was co-transfected into HEK293 cells. Packaging was completed after 72 hours of infection. The culture medium supernatant was harvested and cells were precipitated. PEG8000 was used to precipitate the

virus in the culture medium supernatant. The culture medium supernatant was filtered with 0.45 μm filter membrane and the virus was purified by the iodoxanol method.

AAV injection into rat brains *in vivo* was performed as previously described (Bao et al., 2020). Briefly, the rats were anesthetized by 3% sodium pentobarbital (2 mL/kg) and then injected with 2 μL of AAV-NOX4 or AAV-CON (1×10^{13} IU/ μL) in the basal ganglia using microliter syringes (5 μL , High Pigeon Industry) with a stereo locator and micro-injection pump over 30 minutes (1.5 mm for the anterior fontanelle, 3.5 mm for the side and 6.0 mm for the depth). The needle was held for 3 minutes after injection to prevent backflow and then slowly withdrawn. Rats were placed on an electric blanket; after they woke up from the anesthesia, they were returned to their cages where they were given the same food and water as before modeling.

Magnetic resonance imaging

Magnetic resonance imaging (MRI) was performed at several time points (within 24 hours before ICH and 24, 48, 72 and 96 hours after ICH, six rats per group, 30 rats in total) to compare the edema around the bleeding foci of rats in different groups. The rats were intraperitoneally injected with 3% sodium pentobarbital (2 mL/kg) and placed in a rat coil (50 mm, Medcoil, Suzhou, China) in the prone position with the head first. After localization, the brains were scanned. Imaging was performed on a 3.0T MRI system (Philips, Amsterdam, Netherlands) and the T2 weighted images were acquired using the following parameters: repetition time/echo time: 2000/163 ms; field of view = 60 \times 60 mm²; matrix = 300 \times 297; slice thickness = 1 mm; slice gap = 0.1; flip angle = 90°.

Western blot analysis

Western blotting was performed as previously described (Liu et al., 2016). At 72 hours after injury, the perfused fresh rat brain (50 mg) was homogenized in 500 μL radio immunoprecipitation assay lysis buffer (Beyotime, Shanghai, China) in a low-temperature homogenizer (P0013B, Beyotime) and placed on ice for 30 minutes. The lysate was centrifuged at 12,000 $\times g$ at 4°C for 15 minutes and the protein concentration of the supernatant was determined by the bicinchoninic acid assay kit (PC0020, Solarbio, Beijing, China). Samples were separated by electrophoresis and transferred to a polyvinylidene fluoride membrane (IPVH00005, Merck) (Zhi et al., 2022). The membrane was blocked in 5% bovine serum albumin for 1–1.5 hours and then incubated with the following primary antibodies at 4°C overnight: rabbit anti-NOX4 antibody (1:5000, Abcam, Cambridge, UK, Cat# ab133303, RRID: AB_11155321), rabbit anti-caspase1 antibody (1:2000, Abcam, Cat# ab207802, RRID: AB_2889889), rabbit anti-caspase4/11 antibody (1:2000, Affinity Biosciences, Lianyungang, China, Cat# AF5130, RRID: AB_2837616), rabbit anti-gasdermin D (GSDMD) antibody (1:3000, Abcam, Cat# ab219800, RRID: AB_2888940), rabbit anti-nuclear factor erythroid2-related factor 2 (Nrf2) (1:3000, Cell Signaling Technology, Shanghai, China, Cat# 12721, RRID: AB_2715528), rabbit anti-Kelch like ECH associated protein 1 (Keap-1) (1:3000, Cell Signaling Technology Cat# 8047, RRID: AB_10860776), mouse anti- β -tubulin (1:5000, Novus, Littleton, CO, USA, Cat# NBP2-26250, RRID: AB_2747762) and rabbit anti- β -actin (1:5000, Servicebio, Wuhan, Hubei Province, China, Cat# GB11001, RRID: AB_2801259). The membranes were washed in 1 \times Tris-buffered saline-Tween 20 three times for 5 minutes each and incubated in the following secondary antibodies at 25°C for 1 hour: HRP, goat anti-rabbit IgG (1:5000, Abbkine, Wuhan, Hubei, China, Cat# A21020, RRID: AB_2876889) and HRP, goat anti-mouse IgG (1:5000, Abbkine, Cat# A21010, RRID: AB_2728771). The membranes were washed in 1 \times TBST three times for 5 minutes each and bands were visualized using Tanon ECL kit (Tanon, Shanghai, China) following the manufacturer's instructions. Bands were quantified by ImageJ software (version 1.8.0.112; National Institutes of Health, Bethesda, MD, USA) (Schneider et al., 2012) and expressions were normalized to β -actin or β -tubulin levels.

Immunofluorescence staining

Immunofluorescence staining was performed as previously (Paul et al., 2019). First, rats were intraperitoneally injected with 3% sodium pentobarbital (2 mL/kg) at 72 hours after injury. Paraformaldehyde was injected into the rat brain through the heart for fixation. The brain tissue was dehydrated and embedded in paraffin, followed by sectioning at a thickness of 4 μm . After dewaxing and hydration, the samples were incubated in blocking solution (P0260, Beyotime) for 1 hour at room temperature and then incubated with the following primary antibodies overnight at 4°C: rabbit anti-NOX4 (1:200, Abcam, Cat# ab133303, RRID: AB_11155321), mouse anti-gial fibrillary acidic protein (GFAP) (1:400, Abcam, Cat# ab4648, RRID: AB_449329), rabbit anti-ionized calcium-binding adapter molecule 1 (Iba-1) (1:400, Abcam, Cat# ab178846, RRID: AB_2636859), mouse anti-NeuN (1:250, Millipore, Billerica, MA, USA, Cat# MAB377, RRID: AB_2298772), rabbit anti-nuclear factor erythroid2-related factor 2 (Nrf2) (1:300, Cell Signaling Technology, Shanghai, China, Cat# 12721, RRID: AB_2715528), rabbit anti-GSDMD (1:300, Abcam, Cat# ab219800, RRID: AB_2888940) and rabbit anti-NeuN antibody (1:200, Proteintech, Chicago, IL, USA, Cat# 26975-1-AP, RRID: AB_2880708). Sections were washed three times with phosphate buffered saline (PBS) and stained with the following secondary antibodies at room temperature for 1 hour: goat anti-mouse IgG H&L (Alexa Fluor® 555) (1:500, Abcam, Cat# ab150118, RRID: AB_2714033), donkey anti-mouse IgG H&L (Alexa Fluor® 647) (1:500, Abcam, Cat# ab150107, RRID: AB_2890037), donkey anti-rabbit IgG H&L (Alexa Fluor® 647) (1:500, Abcam, Cat# ab150075, RRID: AB_2752244), goat anti-mouse IgG H&L (Alexa Fluor® 488) (1:500, Abcam, Cat# ab150113, RRID: AB_2576208) and donkey anti-rabbit IgG H&L (Alexa Fluor® 555) (1:500, Abcam, Cat# ab150062, RRID: AB_2801638). Nuclei were stained with 4',6-diamino-

2-phenylindole (10 µg/mL, C0065, Solarbio) solution for 20–30 minutes. Imaging was performed with an inverted fluorescence microscope (Nikon, Kyoto, Japan). ImageJ software was used to count the number of positive cells around the hematoma.

Nissl staining

Nissl staining was performed as previously described (Xie et al., 2021). Brain sections (4–5 µm thick) were prepared as described above, followed by routine dewaxing into water. The sections were placed in tar purple staining solution and dyed at 56°C for 1 hour (C0117, Beyotime). The sections were then rinsed with deionized water and placed in Nissl differentiation solution for several seconds to 2 minutes (observed under the microscope until the background was nearly colorless). After the slices were dehydrated and transparent, the slices were sealed with neutral resin and kept overnight before observation with an inverted microscope (Leica, Wetzlar, Germany). ImageJ software was used for counting Nissl bodies.

Tissue mitochondria extraction

Mitochondrial extraction from fresh rat brain tissue performed using a kit (C3606, Beyotime) (Mao et al., 2019). First, 100 mg tissue was cut under an ice bath and placed in a 1.5 mL centrifuge tube, followed by washing with PBS. The brain tissue block was cut into very small tissue fragments with scissors. Pre-cooled mitochondrial separation reagent A (10 µL/mg) was added and the mixture was homogenized in an ice bath. Low-temperature centrifugation was performed at 1000 × *g* and 4°C for 5 minutes. The supernatant was transferred to another centrifuge tube and centrifuged at 3500 × *g* and 4°C for 10 minutes. The supernatant was carefully removed the precipitates contained the isolated mitochondria.

JC-1 detection

Mitochondrial membrane potential in rat brain was detected by mitochondrial membrane potential assay kit with JC-1 (C2006, Beyotime) as described previously (C2006, Beyotime) (Ma et al., 2010). After brain tissue mitochondria extraction, JC-1 dyeing solution diluted five times with the JC-1 dyeing buffer. We added 0.1 mL of the purified mitochondria (total protein content, approximately 10–100 µg) to 0.9 mL of the diluted JC-1 staining solution and mixed the sample. A fluorescence spectrophotometer (Thermo Fisher Scientific) was used for analysis (excitation wavelength, 485 nm, emission wavelength, 590 nm).

Evans blue staining

Evans blue staining was performed as described previously (Kamada et al., 2007; Choi et al., 2015). After anesthetizing the rats by 1% pentobarbital sodium (30–40 mg/kg), 2% Evans blue dye (2 mL/kg, Leagene, Beijing, China) was injected into the caudal vein (or femoral vein) for 30 minutes, followed by injection of 200–300 mL of heparin normal saline (0.9% sodium chloride + 20 U/mL heparin sodium) into the heart. The rat was decapitated, the brain was removed for fixation and dehydration, and a general picture was taken. Thereafter, 10–20 µm sections were made with a frozen microtome, and Evans blue permeability was observed under an inverted microscope (Nikon, Kyoto, Japan).

Transmission electron microscopy

Transmission electron microscopy (TEM) was performed as previously described (Liu et al., 2021) using the resin embedding method. Rats were intraperitoneally injected with 3% sodium pentobarbital (2 mL/kg) at 72 hours after ICH, and paraformaldehyde was injected into the brain. Fresh perfused brain tissue was cut into 1 mm³ pieces and quickly immersed in 2.5% glutaraldehyde buffer. The samples were embedded and cured in the oven at 70°C for 8 hours. The samples were then sliced by an ultrathin slicer and dispersed on the loading net, so that the samples for transmission observation could be prepared. Sections were analyzed using a transmission electron microscope (HT7800, Hitachi, Tokyo, Japan), and digital images were taken by Servicebio.

Extraction and culture of primary neurons

Fresh rat brain tissue from 8-week-old rats was used for primary neuron extraction < 1 hour after the rats were sacrificed by carbon dioxide inhalation method (After providing a normal supply of oxygen, the concentration of CO₂ was continuously increased until respiratory and cardiac arrest, the CO₂ replacement rate was 30–70%. Adding carbon dioxide slowly and continuously reduced the anxiety of the rats before death. After the rats stopped breathing, they were kept in the tank for at least 5–6 minutes to confirm death). Rat brains were placed in pre-cooling culture medium Dulbecco's modified Eagle medium: Nutrient Mixture F-12 + 10% fetal calf serum + 200 µL Glutamax (Thermo Fisher Scientific) and exposed under a microscope (Thermo Fisher Scientific). The vascular membrane was carefully removed and part of the cortex was transferred into a small beaker with a small amount of the culture medium. The cortex was cut into 0.5–1 mm³ pieces with scissors and placed on ice for digestion. The cut cortex was transferred to a petri dish, and 1 mL of Accutase (A1110501, Thermo Fisher Scientific) was added; the sample was digested at 37°C for 30 minutes and gently shaken every 5 minutes. The upper digestive juices were gently removed, leaving the digested tissue lumps. Next, 1–1.5 mL of fresh medium was added along with a small amount of DNA enzyme, followed by blowing slowly and gently 10 times, samples were held for 2 minutes and the liquid (including a single suspended cell) was transferred into a 15 mL centrifuge tube. Thereafter, 1–1.5 mL of fresh medium and a small amount of DNA enzyme was added again, and the above procedure was repeated twice. The collected cells were evenly plated into

6-well plates and cultured in special culture medium of 48 mL Neurobasal + 1 mL B27 + 200 µL Glumax (Thermo Fisher Scientific) for neurons 4 hours later.

Mito-Tracker Red CMXRos test in PC-12 cells

Pheochromocytoma (PC-12) cells (Guangzhou Jennio Biotech Co., Ltd., Guangzhou, Guangdong, China, Cat# JNO-774, RRID: CVCL_F659) were cultured to an appropriate density and infected with AAV-CON or AAV-NOX4 about 2 weeks, and then treated with H₂O₂ for 24 hours. The medium was removed, and Mito-Tracker Red Chloromethyl-X-rosamine (Mito-Tracker Red CMXRos) working solution (M9940, Solarbio) was added; cells were incubated at 37°C for 15–30 minutes. The solution was replaced with a 37°C fresh Dulbecco's modified Eagle medium containing 10% fetal calf serum. The medium was removed and samples were washed in PBS for three times for 1 minute each. Next, 4% paraformaldehyde fixative was added for 20–30 minutes, followed by three 5-minute PBS washes. Cells were stained with 4',6-diamino-2-phenylindole (10 µg/mL, C0065, Solarbio) for 10 minutes, followed by three 5-minute PBS washes. Finally, samples were sealed and placed at 4°C. A Nikon inverted fluorescence microscope (Nikon, Kyoto, Japan) was used for observation. ImageJ software was used to count the number of positive cells.

Mitochondria-targeted superoxide dismutase mimetic (Mito-TEMPO) injection *in vivo*

Rats in the Mito-TEMPO group were intraperitoneally injected with 3% sodium pentobarbital (2 mL/kg, Cat# Tc-P8411, Merck), and 2 µL Mito-TEMPO (Cat# HY-112879, MedChemExpress, Monmouth Junction, NJ, USA) (Du et al., 2019) was injected into the basal ganglia using a stereotaxic coordinate. The stereotaxic coordinates were as follows: 1.5 mm for the anterior fontanelle, 3.5 mm for the side and 6.0 mm for the depth; 2 µL Mito-TEMPO was slowly injected into the basal ganglia over 30 minutes using a microsyringe (5 µL, High Pigeon Industry) with a micro-single push injection pump (Longer). The needle was held for 3 minutes after injection to prevent backflow. Bone wax was used to seal the pinhole in the skull and close the wound. In the control group, we used normal saline (2 µL), which was injected in the same way as in the Mito-TEMPO group. The vital signs of the rats were stable during the whole process and anesthesia was maintained. Rats were placed on an electric blanket; after they woke up from the anesthesia, they were returned to their cages where they were given the same food and water as before the modeling.

Modified neurologic severity scores test

The modified neurologic severity score (mNSS) is a comprehensive test of movement, sensation, balance beam, reflex and abnormal movement (Liu et al., 2019). Rats were examined prior to injury and 72 hours post-ICH to study the effects of different treatments on neurological function. Neurological function was scored from 0 to 18 (normal score, 0; maximum defect score, 18), higher scores indicated more serious damage.

Statistical analysis

No statistical methods were used to predetermine sample sizes. However, our sample sizes are similar to those reported in a previous publication (Xie et al., 2020). All data were based on at least three independent experiments. Measurement data are shown as the mean ± standard error of mean (SEM). All statistical analysis was performed using GraphPad software (GraphPad Prism version 7.0.0 for Windows, San Diego, CA, USA, www.graphpad.com). One-way analysis of variance with Dunnett's multiple comparison tests were used in the statistical analysis. No tests were performed for outliers and no data were excluded from the analysis. *P* < 0.05 was considered statistically significant.

Results

ICH upregulates NOX4 expression in neurons predominantly

After establishment of the rat ICH model, the hemorrhagic focus was evaluated at different time points of ICH by MRI. The strongest edema-dominant effect on the tissue around the hemorrhagic foci was present around 72 hours after ICH; the edema and occupying effect were reduced after 72 hours (Figure 1A). To identify whether NOX4 expression after ICH is related to the edema occupying effect around the bleeding foci, we evaluated NOX4 expression at different time points in the brain of rats in the same group by immunofluorescence staining. NOX4 expression was the highest around 72 hours and was proportional to the magnitude of the edema occupying effect around the hemorrhagic foci (Figure 1A). To confirm the timing of NOX4 expression increase, western blotting and immunohistochemical staining were performed. The results showed that NOX4 expression was the highest at 72 hours after ICH in rats (Figure 1B–E).

Having clarified the temporal orientation of NOX4, we further explored the spatial orientation of NOX4. A previous study reported that NOX4 is expressed in almost cells of the nervous system (Nayernia et al., 2014). Immunofluorescence staining revealed that NOX4 was the highest in neurons after ICH (Additional Figure 1A–E).

NOX4 knockdown relieves oxidative stress and improves neuronal tolerance to oxidative stress after ICH

Our results showed that NOX4 expression increased after ICH. To investigate the role of NOX4 function after ICH, we used AAV expressing shRNA against NOX4 to knockdown the expression of NOX4 (Additional Figure 2A–G). We then performed ICH modeling in rats injected with AAV-NOX4 (1 × 10¹³ IU/µL, 2 µL, 2 weeks) (Figure 2A and B) and confirmed the reduction in NOX4 mRNA levels in the AAV-NOX4 group (Figure 2C).

Increased NOX4, which is the main source of ROS, causes oxidative stress reaction in the brain (Jung et al., 2016). Compared with the sham group, the ICH group showed markedly increased ROS level in the brain, while AAV-NOX4 prevented the up-regulation of ROS (Figure 2D). Our results showed that NOX4 was most significantly elevated in neurons after ICH. Therefore, we next examined if NOX4 knockdown improved the neuronal tolerance to oxidative stress after ICH by performing western blot analysis for antioxidant proteins

Nrf2 and Keap-1. Nrf2 and Keap-1 levels were both decreased in rat brain after ICH, and their expressions were increased with NOX4 knockdown (Figure 2E–G). Immunofluorescence staining revealed that the immunopositivity of Nrf2 in neurons of ICH rat brain treated with AAV-NOX4 was increased compared with that in the ICH + AAV-CON group (Figure 2H and I). Therefore, these findings indicated that NOX4 knockdown inhibits ROS production and oxidative stress and improves the neuronal tolerance to oxidative stress after ICH.

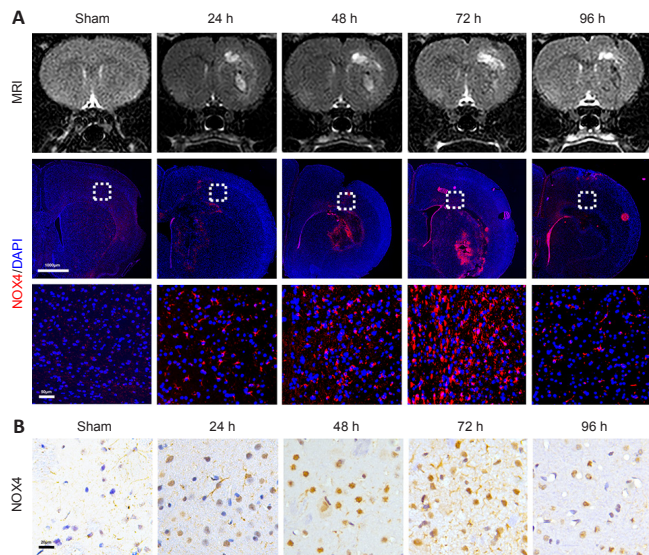


Figure 1 | NOX4 expression reaches the peak at 72 hours in the brain after intracerebral hemorrhage (ICH) in rats. (A) MRI of rat brain at four time points (24, 48, 72, 96 hours) and the corresponding immunofluorescence expression of NOX4 (red) after ICH in rats. Images of selected regions (middle row, white squares) are shown at a higher magnification (bottom row). Compared with the other four groups, the 72 h group had the largest cerebral hemorrhage edema and the highest NOX4 expression. Scale bars: 1000 μ m or 50 μ m. (B) Representative immunohistochemical images of NOX4 expression at four time points (24, 48, 72, 96 hours) after ICH. NOX4 expression was highest in the 72 h group compared with the other four groups. Scale bars: 20 μ m. (C) Percentage of NOX4 positive cells in rat brain from B. (D) Western blot analysis of NOX4 expression in rat brain after ICH in the perilesional basal ganglia at 24, 48, 72 and 96 hours following injury. (E) Quantitative analysis of NOX4 protein levels from D. Data are expressed as the mean \pm SEM ($n = 3$ per group). * $P < 0.05$, *** $P < 0.001$ (one-way analysis of variance with Dunnett's multiple comparison test). ICH: Intracerebral hemorrhage; MRI: magnetic resonance imaging; NOX4: nicotinamide adenine dinucleotide phosphate oxidase 4.

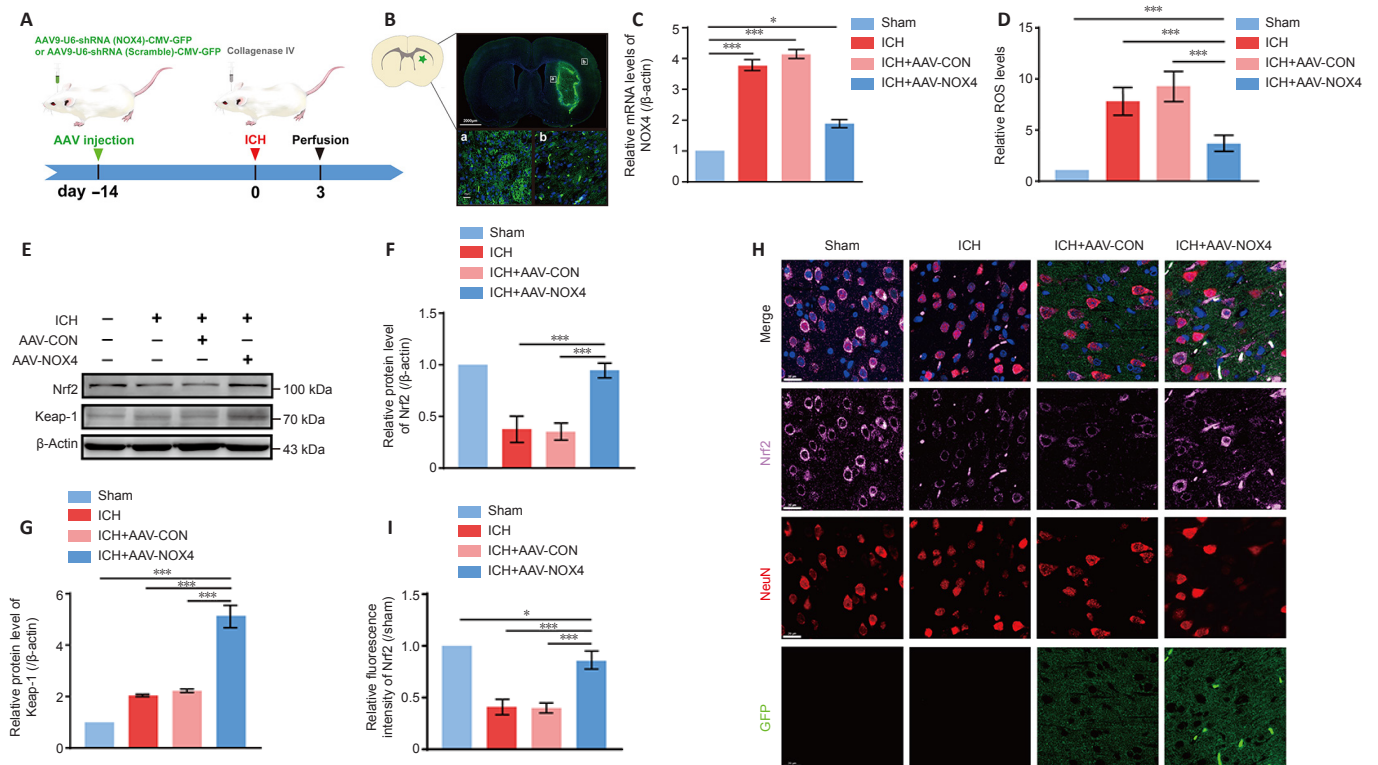
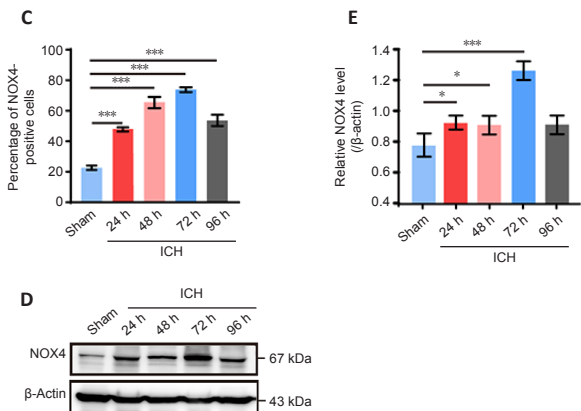


Figure 2 | NOX4 knockdown relieves oxidative stress and enhances the neuronal tolerance to oxidative stress after intracerebral hemorrhage (ICH). (A) Schematic of AAV injection and ICH modeling in rats. (B) Fluorescence images of rat brain with AAV-NOX4 treatment (green). Selected regions (white squares) are shown at a higher magnification (a and b). Scale bars: 2000 μ m or 20 μ m. (C) Relative mRNA level of NOX4 (normalized by levels in the sham group) in rat brain with AAV-NOX4 or AAV-CON treatment before ICH. (D) Relative reactive oxygen species (ROS) levels (normalized by levels in the sham group) after NOX4 knockdown ($n = 5$ per group). (E) Western blot analysis of Nrf2 and Keap-1 expression of ICH rats in the indicated groups. (F, G) Quantitative analysis of Nrf2 (F) and Keap-1 (G) protein levels (normalized to levels in the sham group) as shown in E ($n = 4$ per group). (H) Representative immunofluorescence images of Nrf2 (pink) and NeuN (red) in ICH rats treated by AAV-CON/AAV-NOX4 (green, GFP) as indicated. The expression of Nrf2 in neuron in the ICH and ICH + AAV-CON groups were decreased, while that in the ICH + AAV-NOX4 group was increased. Scale bars: 20 μ m. (I) Relative fluorescence intensity of Nrf2 (normalized by levels in the sham group) after treatment as indicated ($n = 5$ per group). Data are expressed as the mean \pm SEM. * $P < 0.05$, *** $P < 0.001$ (one-way analysis of variance with Dunnett's multiple comparison test). AAV-CON: AAV9-U6-shRNA (Scramble)-CMV-GFP; AAV-NOX4: AAV9-U6-shRNA (NOX4)-CMV-GFP; ICH: intracerebral hemorrhage; Keap-1: Kelch like ECH associated protein 1; NOX4: nicotinamide adenine dinucleotide phosphate oxidase 4; Nrf2: nuclear factor erythroid2-related factor 2; ROS: reactive oxygen species.

Knockdown of NOX4 reduces cerebral edema and neuronal pyroptosis after ICH

We next examined the effects of NOX4 knockdown on neuronal and neurological function injury following SBI after ICH. MRI of rats treated with AAV-CON or AAV-NOX4 was performed (Figure 3A) and the brain water content of rats were measured (Figure 3B). The results showed that the edematous area around the bleeding lesion and the water content of the rat brains with ICH were reduced after NOX4 knockdown. The occurrence and development of cerebral edema is closely related to the permeability of the BBB (Zhang et al., 2020). Therefore, we used Evans blue staining to test BBB permeability at 72 hours after ICH. The leakage of Evans blue dye in the NOX4 knockdown group was significantly reduced, indicating that NOX4 knockdown alleviated the damage to the BBB permeability after ICH (Figure 3C and D).

Considering that NOX4 was mainly increased in the neurons after ICH, we performed Nissl staining. The results showed that ICH disrupted the normal form of neurons, while NOX4 knockdown prevented these effects and downregulated the number of Nissl bodies (Figure 3E and F). We further assessed neurological function after NOX4 knockdown in rats using mNSS. We found that NOX4 knockdown effectively prevented neurological deficit caused by ICH in rats (Figure 3G).

A previous study demonstrated a role for NOX4 in reducing neuronal apoptosis (Kleinschmitz et al., 2010), but whether NOX4 is involved in other types of cell death is unknown. Unlike apoptosis (Luo et al., 2022), during pyroptosis, the nucleus does not shrink and the cells swell and blister until their membranes rupture (Li et al., 2020). We extracted brain tissues before and after ICH for TEM analysis and found that the neurons in ICH model rats showed obvious signs of pyroptosis, however, this injury was not observed in the AAV-NOX4 group (Figure 3H). There was no significant change in the nucleus of neurons

after ICH, but the cell membrane ruptured and the cytoplasmic contents poured out; in contrast, the cell membranes of rats treated with AAV-NOX4 were intact. We further extracted and cultured primary neurons before and after treatment. Under the light microscope, the cell membranes of the neurons in the ICH group exhibited a bubbling phenomenon, while most cell membranes of the neurons in the AAV-NOX4 group were smooth and intact (Figure 3I). Together, these findings demonstrated that knockdown of NOX4 alleviated SBI after ICH, including cerebral edema, neurological impairment and neuronal pyroptosis.

Knockdown of NOX4 reduces neuronal pyroptosis through caspase1/GSDMD-N and caspase4/11/GSDMD-C pathways after ICH

We demonstrated that NOX4 knockdown can reduce neuronal pyroptosis after ICH, but the exact pathways were unknown. We examined the expression of pyroptosis-related proteins by western blot and found that the pyroptosis promoter protein caspase1, specific protein caspase4/11 and GSDMD were significantly increased after ICH (Figure 4A-H), especially caspase4/11, which was cleaved after ICH and the cleaved protein expression was significantly increased. Levels of the N-terminal and C-terminal of the pyroptosis-specific protein GSDMD were significantly increased after ICH. All these phenomena were reversed with NOX4 knockdown. We also detected the expression of GSDMD in neurons by immunofluorescence staining and immunohistochemical staining (Figure 4I-L). GSDMD expression in neurons was elevated after ICH, whereas the expression of GSDMD tended to be normal with NOX4 knockdown.

Together, these results suggested that knockdown of NOX4 reduces neuronal pyroptosis through the caspase1/GSDMD-N and caspase4/11/GSDMD-C pathways after ICH.

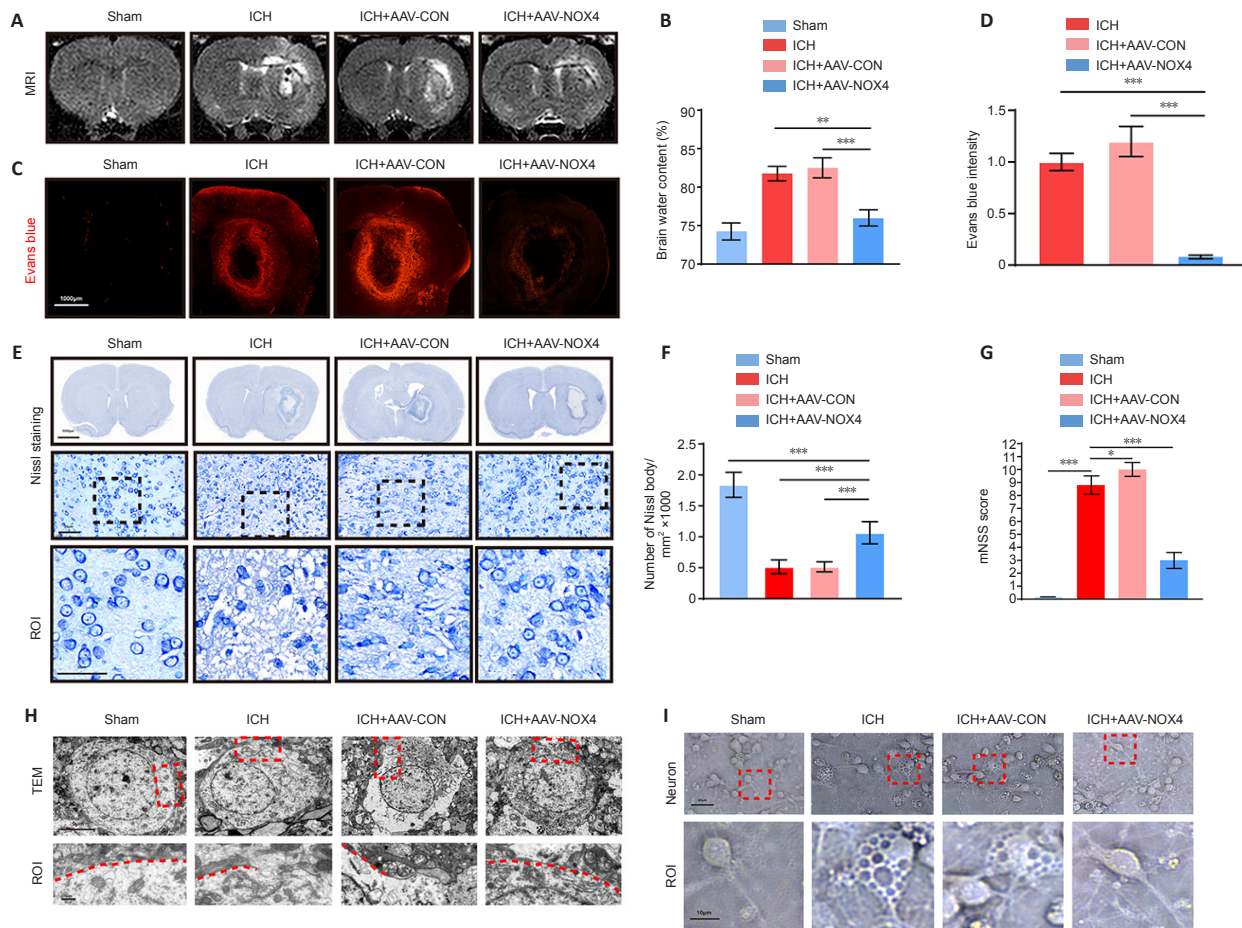


Figure 3 | Knockdown of NOX4 reduces cerebral edema and neuronal pyroptosis after intracerebral hemorrhage (ICH).

(A) MRI of rat brains in the four groups (sham, ICH, ICH + AAV-CON, ICH + AAV-NOX4). The peribleeding edema was aggravated in the ICH and ICH+AAV-CON groups and alleviated in the ICH + AAV-NOX4 group. (B) The brain water content of rat brains evaluated using Evans blue staining ($n = 6$ per group). (C) Evans blue staining of AAV-treated rat brains in four groups (sham, ICH, ICH + AAV-CON, ICH + AAV-NOX4). Evans blue dye leakage was aggravated in the ICH and ICH + AAV-CON groups and was alleviated in the ICH + AAV-NOX4 group. Scale bars: 1000 μm . (D) Evans blue intensity in different groups ($n = 5$ per group). (E) Nissl staining of rat brains in the four groups (sham, ICH, ICH + AAV-CON, ICH + AAV-NOX4). Images of selected regions (black squares) are shown at a higher magnification. The number of Nissl bodies was reduced and the neurons were severely damaged in the ICH and ICH + AAV-CON groups; in the AAV-NOX4 group, the number of Nissl bodies and the morphology of neurons tended to be normal. Scale bars: 1000 μm , 50 μm , 20 μm . (F) Number of Nissl bodies ($n = 5$ per group). (G) mNSS in the four treatment groups ($n = 6$ per group). (H) TEM images of neurons in ICH rats in the four groups (sham, ICH, ICH + AAV-CON, ICH + AAV-NOX4). Images of selected regions (red squares) are shown at a higher magnification. Integrity of the neuronal membrane is shown by red lines. The membrane of neurons in ICH and ICH+AAV-CON groups was broken, while the membrane of neurons in ICH + AAV-NOX4 group was intact. Scale bars: 5 μm or 1 μm . (I) Images of primary neurons in ICH rats in the four groups under a light microscope. Images of selected regions (red squares) are shown at a higher magnification. Many vacuoles were found in the neurons of ICH and ICH + AAV-CON groups, and the cell membrane was damaged; no vacuoles were generated in the ICH + AAV-NOX4 group, and the cell membrane was smooth. Scale bars: 50 μm or 10 μm . Data are expressed as the mean \pm SEM. * $P < 0.05$, ** $P < 0.01$, *** $P < 0.001$ (one-way analysis of variance with Dunnett's multiple comparison test). AAV-CON: AAV9-U6-shRNA (Scramble)-CMV-GFP; AAV-NOX4: AAV9-U6-shRNA (NOX4)-CMV-GFP; ICH: intracerebral hemorrhage; mNSS: modified neurological severity scores; MRI: magnetic resonance imaging; NOX4: nicotinamide adenine dinucleotide phosphate oxidase 4; ROI: region of interest; TEM: transmission electron microscopy.

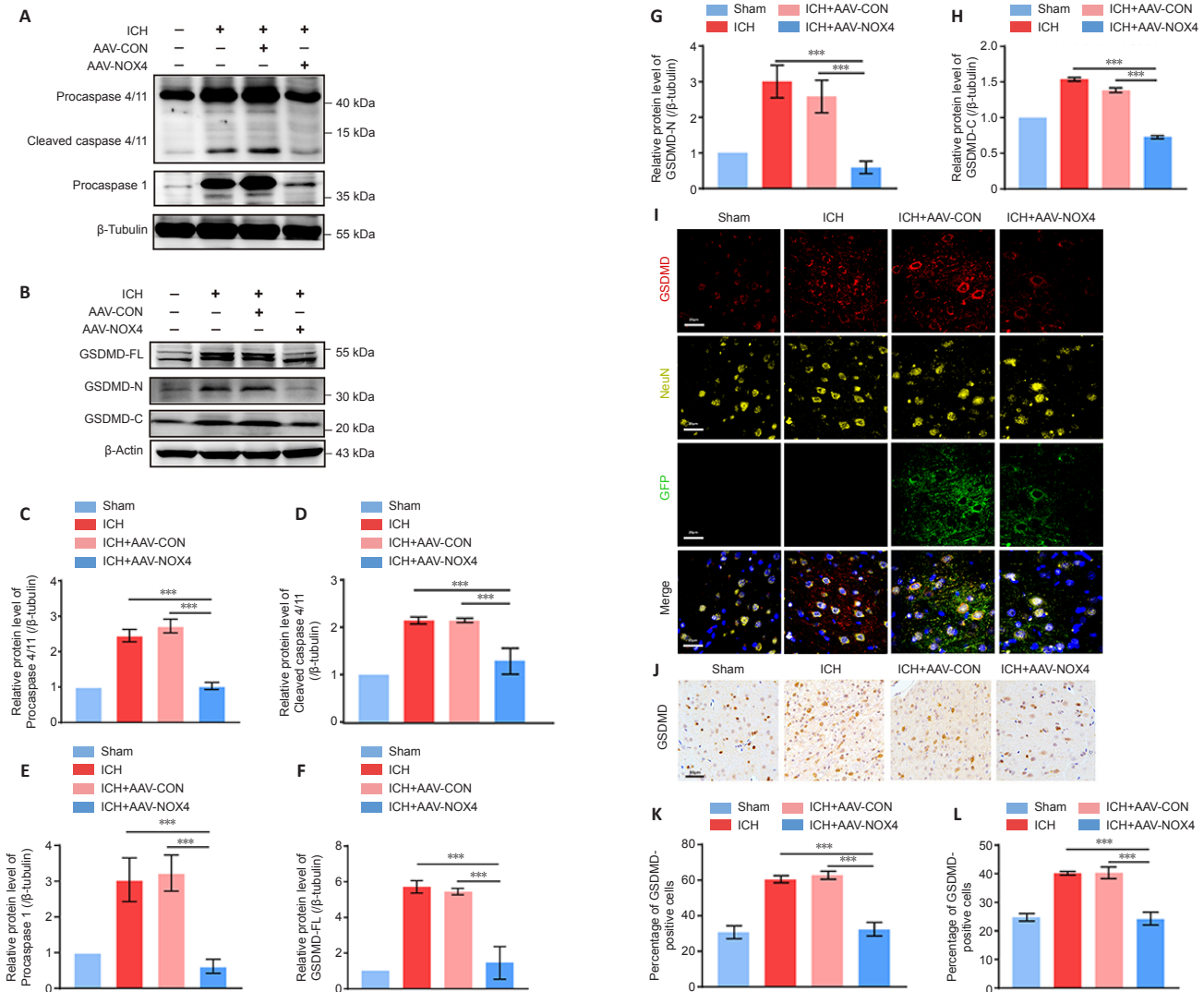


Figure 4 | Knockdown of NOX4 ameliorates neuronal pyroptosis through caspase 1/GSDMD-N and caspase4/11/GSDMD-C pathways after ICH. (A) Western blot analysis of Procaspase4/11, Cleaved caspase4/11 and Procaspase1 expression in the indicated groups. (B) Western blot analysis of GSDMD-FL, GSDMD-N and GSDMD-C expression in the indicated groups. (C–H) Quantitative analysis of Procaspase4/11 (C), Cleaved caspase4/11 (D), Procaspase1 (E), GSDMD-FL (F), GSDMD-N (G) and GSDMD-C (H) protein levels shown in A and B ($n = 4$ per group). (I) Representative immunofluorescence images showing the immunoreactivity of GSDMD (red) in neurons (NeuN-positive cells, yellow) in the indicated groups (AAV, GFP, green). The expression of GSDMD in the ICH and ICH + AAV-CON groups was increased, while that in the ICH + AAV-NOX4 group was decreased. Scale bars: 20 μm . (J) Representative immunohistochemical images illustrate the changes in the GSDMD protein expression in the indicated groups. The expression of GSDMD in the ICH and ICH + AAV-CON groups was increased, while that in the ICH + AAV-NOX4 group was decreased. Scale bars: 50 μm . (K, L) Percentage of GSDMD-positive cells in immunofluorescence (K) and immunohistochemical (L) images ($n = 5$ per group). Data are expressed as the mean \pm SEM. *** $P < 0.001$ (one-way analysis of variance with Dunnett's multiple comparison test). AAV-CON: AAV9-U6-shRNA (Scramble)-CMV-GFP; AAV-NOX4: AAV9-U6-shRNA (NOX4)-CMV-GFP; GSDMD: gasdermin D; ICH: intracerebral hemorrhage; MRI: magnetic resonance imaging; NOX4: nicotinamide adenine dinucleotide phosphate oxidase 4.

NOX4 knockdown improves neuronal mitochondrial function by reducing NOX4 expression and ROS production in the mitochondria after ICH

Mitochondria are the main source of intracellular ROS and produce approximately 90% of ROS in cells (Zhang et al., 2019; Zhang and Wong, 2021). A previous study only measured NOX4 and ROS levels in tissues (Morioka et al., 2018). To further accurately assess the changes of NOX4 and ROS in mitochondria after ICH, we extracted mitochondria from tissues and performed western blot. The results showed that NOX4 expression in mitochondria (Mito-NOX4) was increased after ICH, and AAV-NOX4 successfully reduced NOX4 expression in the mitochondria, consistent with the overall NOX4 expression trend (Figure 5A and B). TEM was used to observe the changes in the mitochondria of neurons of different treatment groups. The mitochondria were severely damaged after ICH, with loss of mitochondrial shape, and the number of mitochondrial cristae was severely reduced; these effects were not observed in the AAV-NOX4 treatment group (Figure 5C and D). We further investigated the changes in the mitochondrial membrane potential using JC-1. The results showed that the ratio of JC-1 monomer/polymer in the mitochondria increased after ICH, indicating mitochondrial membrane depolarization and mitochondria damage; in the AAV-NOX4 group, these effects were not observed (Figure 5E).

Because mitochondrial ROS content in brain tissues could not be specifically detected, we simulated a cell model after oxidative stress stimulation. PC-12 cells, commonly used to simulate neuron cell lines (Liu et al., 2020), were transfected with AAV-NOX4 and stimulated by H₂O₂, followed by staining with MitoTracker Red CMXRos. The fluorescence intensity of MitoROS in PC-12 cells transfected with AAV-NOX4 was significantly lower than that in the oxidative

stress treatment group, which was consistent with the previous results (Figure 5F and G). Together, these results suggested that NOX4 knockdown reduced NOX4 in the mitochondria and reduced ROS expression, thus improving neuronal mitochondrial function after ICH.

Mito-TEMPO reduces neuronal pyroptosis and mitochondria oxidative stress after ICH

Oxidative stress stimulates an increase in ROS in the mitochondria, causing further damage (Shu et al., 2020). In this study, we found that the ICH-mediated increased ROS in the mitochondria of brain tissues was significantly decreased by treatment with AAV-NOX4 in advance. Hence, reducing ROS in the mitochondria after ICH is particularly important for alleviating SBI. To further verify whether AAV-NOX4 can alleviate SBI after ICH by inhibiting ROS in the mitochondria, we used Mito-TEMPO (a specific inhibitor of mitochondrial ROS).

Evans blue staining revealed that Mito-TEMPO had the same improvement effect on BBB permeability as observed in the AAV-NOX4 group after ICH (Figure 6A and B). To determine whether the inhibitory effect of Mito-TEMPO on ROS is related to NOX4 in mitochondria, western blot analysis was performed, the results showed that Mito-TEMPO reduced NOX4 expression in the mitochondria (Figure 6C and D). Nissl staining showed that the death of neurons was reduced by Mito-TEMPO after ICH, similar to the AAV-NOX4 group (Figure 6E and F). Numerous studies have reported that mitochondrial H₂O₂ production is induced by NOX4 (Hirschhäuser et al., 2015). We also evaluated mitochondrial H₂O₂ content in the brain tissues after ICH and found that the H₂O₂ content in the mitochondria of brain tissues was reduced in

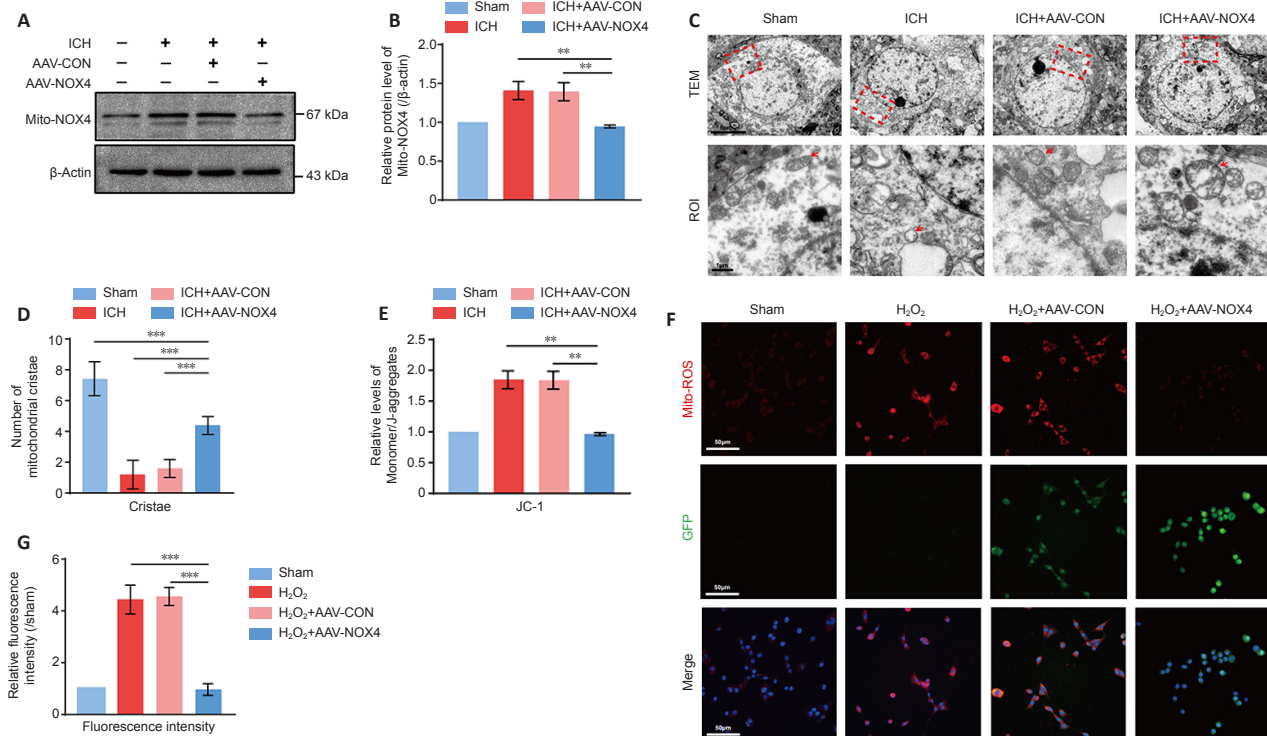


Figure 5 | NOX4 knockdown reduces the NOX4 expression and reactive oxygen species (ROS) production in mitochondria, and improves neuronal mitochondrial function after intracerebral hemorrhage (ICH).

(A) Western blot analysis of mitochondrial NOX 4 (Mito-NOX4) expression in the indicated groups. (B) Quantitative analysis of Mito-NOX4 protein levels (normalized by levels in the sham group) shown in A ($n = 4$ per group). (C) Images of neuron mitochondria in the indicated groups under the TEM. Images of selected regions (red squares) are shown at a higher magnification. Red arrows indicate the mitochondria of different treatment groups. The mitochondria in the ICH and ICH + AAV-CON groups were severely damaged and mitochondrial crest was reduced; these effects were not observed in the ICH + AAV-NOX4 group. Scale bars: 5 μm or 1 μm . (D) The number of mitochondrial cristae in different groups ($n = 5$ per group). (E) Comparison of mitochondrial membrane potential (JC-1) among different groups ($n = 5$ per group). (F) Representative immunofluorescence images showing the immunoreactivity of Mito-ROS (red) in PC-12 cells infected with AAV-CON or AAV-NOX4 (green, GFP) after treatment with H₂O₂. Mito-ROS in the H₂O₂ and H₂O₂ + AAV-CON groups was increased, while that in the H₂O₂ + AAV-NOX4 group was decreased. Scale bars: 50 μm . (G) The fluorescent intensity of mitochondrial ROS in different groups shown in (F) ($n = 5$ per group). Data are expressed as the mean \pm SEM. ** $P < 0.01$, *** $P < 0.001$ (one-way analysis of variance with Dunnett's multiple comparison test). AAV-CON: AAV9-U6-shRNA (Scramble)-CMV-GFP; AAV-NOX4: AAV9-U6-shRNA (NOX4)-CMV-GFP; ICH: intracerebral hemorrhage; Mito-ROS: ROS in mitochondria; NOX4: nicotinamide adenine dinucleotide phosphate oxidase 4; TEM: transmission electron microscopy.

both AAV-NOX4 and Mito-TEMPO groups after ICH (Figure 6G). Finally, we compared the improvement in neuronal pyroptosis after AAV-NOX4 and Mito-TEMPO treatment and observed that both treatment groups demonstrated reduced expression of GSDMD after ICH, indicating that the effect of AAV-NOX4 and Mito-TEMPO on neuronal pyroptosis was equivalent (Figure 6H and I). Therefore, Mito-TEMPO can reduce neuronal pyroptosis and mitochondria oxidative stress after ICH, and NOX4 may be an important potential target of Mito-TEMPO.

Discussion

ICH is not only related to the hematoma itself, but also to the SBI around the hematoma (Chen et al., 2015). Treatment to repair the damaged nervous system after ICH has become the primary concern of researchers. In this study, we explored ROS production and the neuronal response to oxidative stress after NOX4 knockdown. We also explored the role of NOX4 in neuronal pyroptosis and mitochondrial oxidative stress, along with the underlying mechanism. We showed that NOX4 expression of neurons was significantly increased after ICH. Knockdown of NOX4 relieved oxidative stress and improved neuronal tolerance to oxidative stress after ICH. Knockdown of NOX4 also ameliorated neuronal cell death by reducing neuronal pyroptosis through the caspase1/GSDMD-N and caspase4/11/GSDMD-C pathways. Additionally, NOX4 knockdown reduced NOX4 expression in the mitochondria and reduced ROS production, which improved neuronal mitochondrial function and alleviated the cycle of ROS accumulation after ICH. We used a mitochondrion-specific ROS inhibitor (Mito-TEMPO) to explore the relationship between ROS and NOX4 by investigating the reverse effect of ROS on NOX4 in mitochondria. We found that Mito-TEMPO inhibited the expression of NOX4 and neuronal pyroptosis, with the same effects of AAV-NOX4.

The presence of NOX4 is a double-edged sword, as while it is essential for the signal transduction of ROS, its abnormal expression can cause damage to tissue (Radermacher et al., 2013). In this regard, diabetes (Østergaard et al., 2022), liver fibrosis (Zhou et al., 2022), heart failure (Kuroda and Sadoshima, 2010), and brain injury (Casas et al., 2017) have been studied, but there are few studies on ICH. Continuing from our previous study, we found that NOX4 knockdown effectively reduced the oxidative stress response of neurons after ICH. We explored the impact of NOX4 on neuronal tolerance to oxidative stress and found that NOX4 knockdown not only weakened the oxidative stress response but also significantly increased the content of Nrf2 and Keap-

1, which are two important antioxidant proteins, indicating that it effectively enhanced the neuronal tolerance to oxidative stress.

Many previous studies have reported the role of NOX4 in apoptosis. Apoptosis is a type of programmed cell death during embryonic development and a self-renewal pattern of cells in healthy tissues (Jeng et al., 2010; Gong et al., 2022; Yan et al., 2022). In apoptosis, cysteine proteases neither release the cytoplasmic contents out of the cell nor cause any inflammatory response after inducing lysis of the cell matrix, DNA cleavage and plasma membrane contraction. Unlike apoptosis, pyroptosis is a type of inflammatory necrosis and programmed cell death. Pyroptosis has been observed in many types of cells, such as monocytes, macrophages, dendritic cells and many other cell types (Reisetter et al., 2011). Therefore, we focused on the process of neuronal pyroptosis stimulated by oxidative stress and the role of NOX4 in this process after ICH. Our results showed that NOX4 knockdown effectively reduced neuronal pyroptosis through caspase1 and caspase4/11 pathways. Caspase1 and caspase4/11 interact with cleaved GSDMD-N and GSDMD-C, respectively, to co-regulate neuronal pyroptosis after ICH.

ROS produced by the NOX system not only directly leads to excessive production and accumulation of ROS in and outside the cells, but also acts on the mitochondria and other ROS-related enzyme systems (such as the mitochondrial electron transport chain) (Wilkinson-Berka et al., 2013). This can lead to abnormal functioning of the mitochondria, resulting in the production of secondary ROS. These secondary ROS, together with the primary ROS produced by NOX, can restimulate the mitochondria and create a circle of oxidative stress in the tissues (Marzetti et al., 2013), because of the anti-reactive oxygen therapy cannot fundamentally eliminate the production of ROS, resulting in the uncontrolled production of ROS, which ultimately lead to the progression of the pathological process. No ROS scavenger or ROS inhibitor has been shown to be a promising treatment for stroke in animal studies or has been successfully applied in the clinic (Bao et al., 2018). Studies have found that oxidative stress after ICH increases the ROS levels in the mitochondria, which is likely to trigger the cycle mentioned above. We found that NOX4 expression was also elevated in mitochondria after ICH. TEM and other experiments were used to observe the damage of mitochondria after ICH, and it was found that the mitochondria were less affected to a certain extent after NOX4 knockdown. Mito-TEMPO, a mitochondria-specific ROS inhibitors, exhibited similar effects with AAV-NOX4. Therefore, we hypothesized that NOX4 may be regulated by Mito-TEMPO. To verify our

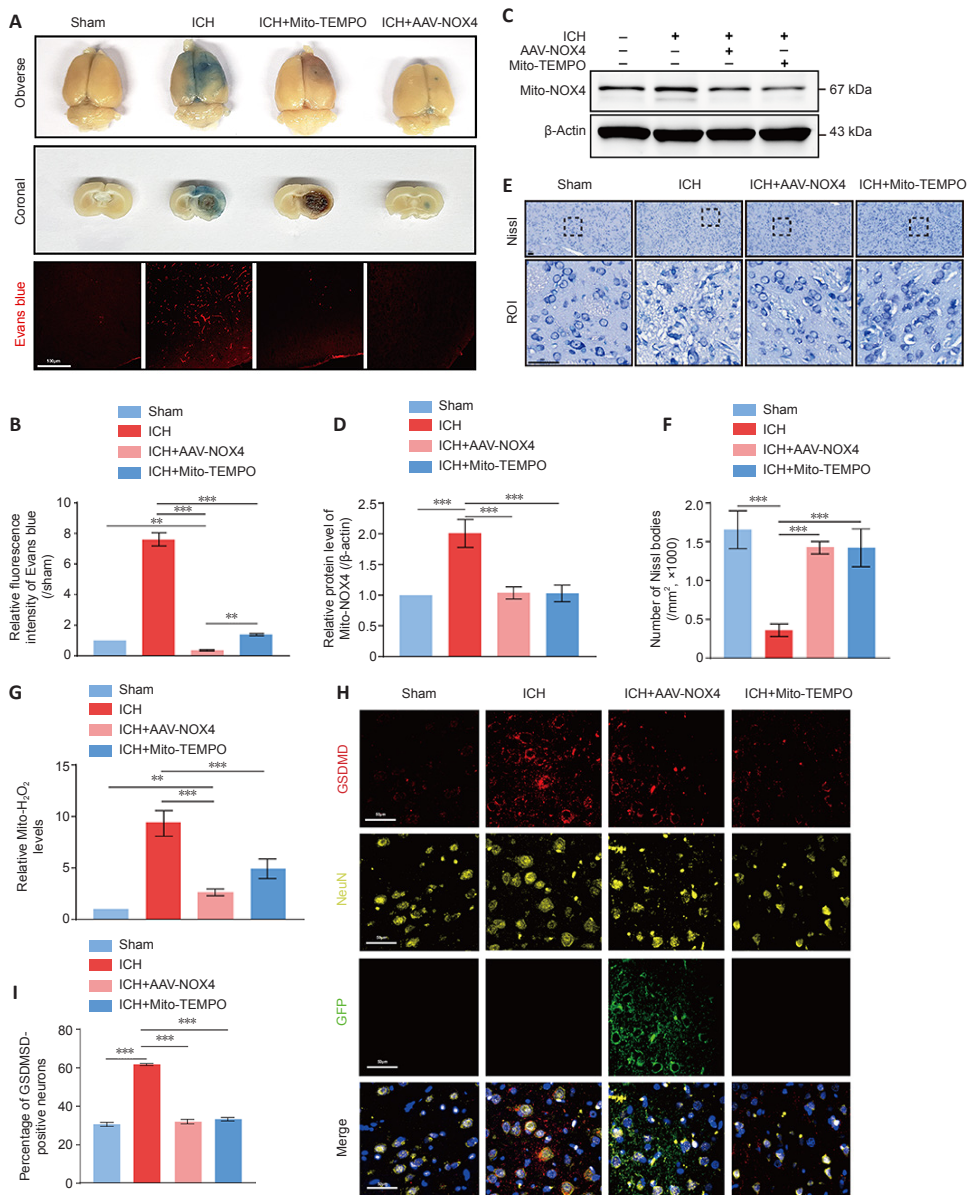


Figure 6 | Mito-TEMPO reduces neuronal pyroptosis and oxidative stress response after intracerebral hemorrhage (ICH).

(A) Evans blue staining following application of the mitochondrial ROS inhibitor Mito-TEMPO and treatment as shown in the indicated groups. Evans blue dye leakage was the strongest in the ICH group; leakage was not observed in the ICH + AAV-NOX4 and ICH + Mito-TEMPO groups, both under naked eye and fluorescence microscope. Scale bars: 100 μm. (B) Relative fluorescence intensity (normalized by levels in the sham group) of Evans blue ($n = 5$ per group). (C) Western blot analysis of Mito-NOX4 expression in the brain of ICH rats treated by AAV-NOX4 or Mito-TEMPO. (D) Relative protein levels (normalized by levels in the sham group) of Mito-NOX4 shown in C ($n = 4$ per group). (E) Nissl staining of rat brain in the indicated groups. The ICH group had the fewest Nissl bodies and the most serious neuron morphology damage; this was not observed in the ICH + AAV-NOX4 and ICH + Mito-TEMPO groups. Scale bars: 50 μm. (F) Quantitative analysis of the number of Nissl bodies shown in E ($n = 5$ per group). (G) Relative Mito-H₂O₂ levels (normalized by levels in the sham group) of mitochondria after treatment with AAV-NOX4 or Mito-TEMPO ($n = 5$ per group). (H) Representative immunofluorescence images illustrate the changes in GSDMD (red) expression of neurons (NeuN-positive cells, yellow) of ICH rats after treatment with AAV-NOX4 (green, GFP) or Mito-TEMPO. The expression of GSDMD in the ICH group was increased, while that in the ICH + AAV-NOX4 and ICH + Mito-TEMPO groups was decreased. Scale bars: 50 μm. (I) Percentage of GSDMD-positive cells among neurons after treatment with AAV-NOX4 or Mito-TEMPO ($n = 5$ per group). Data are expressed as means ± SEM. $^{**}P < 0.01$, $^{***}P < 0.001$ (one-way analysis of variance with Dunnett's multiple comparison test). AAV-NOX4: AAV9-U6-shRNA (NOX4)-CMV-GFP; GSDMD: gasdermin D; ICH: intracerebral hemorrhage; Mito-H₂O₂: H₂O₂ in mitochondria; Mito-NOX4: NOX4 in mitochondria; Mito-TEMPO: mitochondria-targeted superoxide dismutase mimetic; NOX4: nicotinamide adenine dinucleotide phosphate oxidase 4.

hypothesis, we evaluated the protein levels of NOX4 in mitochondria after AAV-NOX4 and Mito-TEMPO treatment and found that the NOX4 content in the mitochondria was decreased after treatment with Mito-TEMPO. We speculate that NOX4 may be an important target of Mito-TEMPO and may eliminate the excessive production of ROS in brain tissues after ICH. Together, these results may help facilitate the clinical development of NOX4 inhibitors in the treatment of ICH.

This study has several limitations. We only focused on neurons in the present study, and the effect of NOX4 on other nerve cells after ICH remains to be further explored. Our results support the crucial role of NOX4 in neuronal pyroptosis following ICH, but how NOX4 interacts with pyroptosis related proteins needs further exploration. Moreover, the exact site of NOX4 interacts with Mito-TEMPO exactly are still unknown, it will be the focus of our future study.

In summary, our findings indicate that NOX4 is an important factor mediating the pathophysiological development of ICH in rats. We found that NOX4 knockdown significantly enhanced the neuronal tolerance to oxidative stress and reduced neuronal pyroptosis and mitochondrial oxidative stress, thus protecting the function of mitochondria and the BBB after ICH. NOX4 downregulation improved the neuronal tolerance to oxidative stress, indicating that NOX4 may be a therapeutic target for antioxidant therapy. Furthermore, our results suggest that NOX4 may be an important therapeutic target in ICH, providing valuable evidence for the feasibility of NOX4-targeted therapy strategies during the critical period of ICH and further highlighting the importance of NOX4-specific inhibitor development. Drugs targeting NOX4 will be an innovative treatment for ICH in the future.

Acknowledgments: We sincerely appreciate professor Ru-Xiang Xu, the Chairman of Nerve Injury and Repair Branch of Chinese Neurological Society,

for helpful discussions and insightful comments regarding this study and the colleagues at the Zhujiang Hospital of Southern Medical University, who participated in this study with great cooperation.

Author contributions: BYD, CNX, and YZC conceived and designed the study. BYD, CNX, JYX, and EHH constructed the animal study and contributed to the acquisition of data. BYD performed the *in vitro* experiments. BYD, CNX, XWF, and WJC analyzed the data, BYD wrote the manuscript. BYD, CNX, ZWG, and YZC revised the manuscript. YZC provided reagents, materials and analytical tools. All authors contributed to manuscript revision, read, and approved the final version of this manuscript.

Conflicts of interest: All authors declared that there is no conflict of interest regarding the publication of this article.

Availability of data and materials: All data generated or analyzed during this study are included in this published article and its supplementary information files.

Open access statement: This is an open access journal, and articles are distributed under the terms of the Creative Commons AttributionNonCommercial-ShareAlike 4.0 License, which allows others to remix, tweak, and build upon the work non-commercially, as long as appropriate credit is given and the new creations are licensed under the identical terms.

Additional files:

Additional Figure 1: Cellular localization of NOX4 after ICH.

Additional Figure 2: Construction and screening of adeno-associated virus (AAV).

References

- Bao Q, Hu P, Xu Y, Cheng T, Wei C, Pan L, Shi J (2018) Simultaneous blood-brain barrier crossing and protection for stroke treatment based on edaravone-loaded ceria nanoparticles. *ACS Nano* 12:6794-6805.
- Bao WD, Zhou XT, Zhou LT, Wang F, Yin X, Lu Y, Zhu LQ, Liu D (2020) Targeting miR-124/Ferroptin signaling ameliorated neuronal cell death through inhibiting apoptosis and ferroptosis in aged intracerebral hemorrhage murine model. *Aging Cell* 19:e13235.
- Bergsbaken T, Cookson BT (2007) Macrophage activation redirects yersinia-infected host cell death from apoptosis to caspase-1-dependent pyroptosis. *PLoS Pathog* 3:e161.
- Bergsbaken T, Fink SL, Cookson BT (2009) Pyroptosis: host cell death and inflammation. *Nat Rev Microbiol* 7:99-109.
- Brown GC, Borutaite V (2012) There is no evidence that mitochondria are the main source of reactive oxygen species in mammalian cells. *Mitochondrion* 12:1-4.
- Casas AL, Geuss E, Kleikers PWM, Mencl S, Herrmann AM, Buendia I, Egea J, Meuth SG, Lopez MG, Kleinschnitz C, Schmidt H (2017) NOX4-dependent neuronal autotoxicity and BBB breakdown explain the superior sensitivity of the brain to ischemic damage. *Proc Natl Acad Sci U S A* 114:12315-12320.
- Chen S, Yang Q, Chen G, Zhang JH (2015) An update on inflammation in the acute phase of intracerebral hemorrhage. *Transl Stroke Res* 6:4-8.
- Choi HS, Ahn SS, Shin NY, Kim J, Kim JH, Lee JE, Lee HY, Heo JH, Lee SK (2015) Permeability parameters measured with dynamic contrast-enhanced MRI: correlation with the extravasation of Evans blue in a rat model of transient cerebral ischemia. *Korean J Radiol* 16:791-797.
- Ding R, Chen Y, Yang S, Deng X, Fu Z, Feng L, Cai Y, Du M, Zhou Y, Tang Y (2014) Blood-brain barrier disruption induced by hemoglobin in vivo: Involvement of up-regulation of nitric oxide synthase and peroxynitrite formation. *Brain Res* 1571:25-38.
- Drummond GR, Sobey CG (2014) Endothelial NADPH oxidases: which NOX to target in vascular disease? *Trends Endocrinol Metab* 25:452-463.
- Du K, Ramachandran A, Weemhoff JL, Woolbright BL, Jaeschke AH, Chao X, Ding WX, Jaeschke H (2019) Mito-toxic protective agents against liver injury but induces limited secondary apoptosis during the late phase of acetaminophen hepatotoxicity. *Arch Toxicol* 93:163-178.
- Feng L, Chen Y, Ding R, Fu Z, Yang S, Deng X, Zeng J (2015) P2X7R blockade prevents NLRP3 inflammasome activation and brain injury in a rat model of intracerebral hemorrhage: involvement of peroxynitrite. *J Neuroinflammation* 12:190.
- Gong QY, Cai L, Jing Y, Wang W, Yang DX, Chen SW, Tian HL (2022) Urolithin A alleviates blood-brain barrier disruption and attenuates neuronal apoptosis following traumatic brain injury in mice. *Neural Regen Res* 17:2007-2013.
- Haslund-Vinding J, McBean G, Jaquet V, Vilhardt F (2017) NADPH oxidases in oxidant production by microglia: activating receptors, pharmacology and association with disease. *Br J Pharmacol* 174:1733-1749.
- Hirschhäuser C, Bornbaum J, Reis A, Böhme S, Kaludercic N, Menabò R, Di Lisa F, Boengler K, Shah AM, Schulz R, Schmidt HH (2015) NOX4 in mitochondria: yeast two-hybrid-based interaction with complex I without relevance for basal reactive oxygen species? *Antioxid Redox Signal* 23:1106-1112.
- Hu X, Tao C, Gan Q, Zheng J, Li H, You C (2016) Oxidative stress in intracerebral hemorrhage: sources, mechanisms, and therapeutic targets. *Oxid Med Cell Longev* 2016:3215391.
- Jeng MJ, Soong WJ, Lee YS, Tsao PC, Yang CF, Chiu SY, Tang RB (2010) Meconium exposure mediated cell death and apoptosis in human alveolar epithelial cells. *Pediatr Pulmonol* 45:816-823.
- Jin P, Qi D, Cui Y, Lenahan C, Deng S, Tao X (2022) Activation of LRP6 with HLY78 attenuates oxidative stress and neuronal apoptosis via GSK3 β /Sirt1/PGC-1 α pathway after ICH. *Oxid Med Cell Longev* 2022:7542468.
- Jung YS, Lee SW, Park JH, Seo HB, Choi BT, Shin HK (2016) Electroacupuncture preconditioning reduces ROS generation with NOX4 down-regulation and ameliorates blood-brain barrier disruption after ischemic stroke. *J Biomed Sci* 23:32.
- Kamada H, Yu F, Nito C, Chan PH (2007) Influence of hyperglycemia on oxidative stress and matrix metalloproteinase-9 activation after focal cerebral ischemia/reperfusion in rats: relation to blood-brain barrier dysfunction. *Stroke* 38:1044-1049.
- Kayagaki N, Warming S, Lamkanfi M, Vande Walle L, Louie S, Dong J, Newton K, Qu Y, Liu J, Heldens S, Zhang J, Lee WP, Roose-Girma M, Dixit VM (2011) Non-canonical inflammasome activation targets caspase-11. *Nature* 479:117-121.
- Kleinschnitz C, Grund H, Winkler K, Armistage ME, Jones E, Mittal M, Barit D, Schwarz T, Geis C, Kraft P, Barthel K, Schuhmann MK, Herrmann AM, Meuth SG, Stoll G, Meurer S, Schrewe A, Becker L, Gailus-Durner V, Fuchs H, et al. (2010) Post-stroke inhibition of induced NADPH oxidase type 4 prevents oxidative stress and neurodegeneration. *PLoS Biol* 8:e1000479.
- Kuroda J, Sadoshima J (2010) NADPH oxidase and cardiac failure. *J Cardiovasc Transl Res* 3:314-320.
- Li J, Hao JH, Yao D, Li R, Li XF, Yu ZY, Luo X, Liu XH, Wang MH, Wang W (2020) Caspase-1 inhibition prevents neuronal death by targeting the canonical inflammasome pathway of pyroptosis in a murine model of cerebral ischemia. *CNS Neurosci Ther* 26:925-939.
- Liu L, Fujimoto M, Kawakita F, Nakano F, Imanaka-Yoshida K, Yoshida T, Suzuki H (2016) Anti-vascular endothelial growth factor treatment suppresses early brain injury after subarachnoid hemorrhage in mice. *Mol Neurobiol* 53:4529-4538.
- Liu P, Yu X, Dai X, Zou W, Yu X, Niu M, Chen Q, Teng W, Kong Y, Guan R, Liu X (2021) Scalp acupuncture attenuates brain damage after intracerebral hemorrhage through enhanced mitophagy and reduced apoptosis in rats. *Front Aging Neurosci* 13:718631.
- Liu Y, Wang J, Zhou X, Cao H, Zhang X, Huang K, Li X, Yang G, Shi X (2020) miR-324-5p inhibits C2C12 cell differentiation and promotes intramuscular lipid deposition through lncDUM and PM20D1. *Mol Ther Nucleic Acids* 22:722-732.
- Liu Y, Xue X, Zhang H, Che X, Luo J, Wang P, Xu J, Xing Z, Yuan L, Liu Y, Fu X, Sun S, Zhang H, Wu C, Yang J (2019) Neuronal-targeted TFEF rescues dysfunction of the autophagy-lysosomal pathway and alleviates ischemic injury in permanent cerebral ischemia. *Autophagy* 15:493-509.
- Luo G, Feng R, Li W, Chen Y, Sun Y, Ma J, Duo Y, Wen T (2022) Dcf1 induces glioblastoma cells apoptosis by blocking autophagy. *Cancer Med* 11:207-223.
- Ma J, Zhang L, Li S, Liu S, Ma C, Li W, Falck JR, Manthati VL, Reddy DS, Medhara M, Jacobs ER, Zhu D (2010) 8,9-Epoxyicosatrienoic acid analog protects pulmonary artery smooth muscle cells from apoptosis via ROCK pathway. *Exp Cell Res* 316:2340-2353.
- Mao J, Li Y, Li S, Li J, Tian Y, Feng S, Liu X, Bian Q, Li J, Hu Y, Zhang L, Ji H (2019) Bufei Jianpi granules reduce quadriceps muscular cell apoptosis by improving mitochondrial function in rats with chronic obstructive pulmonary disease. *Evid Based Complement Alternat Med* 2019:1216305.
- Marzetti E, Csizsar A, Dutta D, Balagopal G, Calvani R, Leeuwenburgh C (2013) Role of mitochondrial dysfunction and altered autophagy in cardiovascular aging and disease: from mechanisms to therapeutics. *Am J Physiol Heart Circ Physiol* 305:H459-476.
- Morioka S, Sakaguchi H, Yamaguchi T, Ninouy Y, Mohri H, Nakamura T, Hisa Y, Ogita K, Saito N, Ueyama T (2018) Hearing vulnerability after noise exposure in a mouse model of reactive oxygen species overproduction. *J Neurochem* 146:459-473.
- Nayernia Z, Jaquet V, Krause KH (2014) New insights on NOX enzymes in the central nervous system. *Antioxid Redox Signal* 20:2815-2837.
- Nishimura A, Ago T, Kuroda J, Arimura K, Tachibana M, Nakamura K, Wakisaka Y, Sadoshima J, Iihara K, Kitazono T (2016) Detrimental role of pericyte Nox4 in the acute phase of brain ischemia. *J Cereb Blood Flow Metab* 36:1143-1154.
- Nisimoto Y, Diebold BA, Cosentino-Gomes D, Lambeth JD (2014) Nox4: a hydrogen peroxide-generating oxygen sensor. *Biochemistry* 53:5111-5120.
- Østergaard JA, Jha JC, Sharma A, Dai A, Choi JSY, de Haan JB, Cooper ME, Jandeleit-Dahm K (2022) Adverse renal effects of NLRP3 inflammasome inhibition by MCC950 in an interventional model of diabetic kidney disease. *Clin Sci (Lond)* 136:167-180.
- Paul S, Chhatar S, Mishra A, Lal G (2019) Natural killer T cell activation increases iNOS(+) CD206(-) M1 macrophage and controls the growth of solid tumor. *J Immunother Cancer* 7:208.
- Percie du Sert N, Hurst V, Ahluwalia A, Alam S, Avey MT, Baker M, Browne WJ, Clark A, Cuthill IC, Dirnagl U, Emerson M, Garner P, Holgate ST, Howells DW, Karp NA, Lázic SE, Lidster K, MacCallum CJ, Macleod M, Pearl EJ, et al. (2020) The ARRIVE guidelines 2.0: Updated guidelines for reporting animal research. *PLoS Biol* 18:e3000410.
- Piras BA, Tian Y, Xu Y, Thomas NA, O'Connor DM, French BA (2016) Systemic injection of AAV9 carrying a periostin promoter targets gene expression to a myofibroblast-like lineage in mouse hearts after reperfused myocardial infarction. *Gene Ther* 23:469-478.
- Radermacher KA, Winkler K, Langhauser F, Altenhofer S, Kleikers P, Hermans JJ, Hrabe de Angelis M, Kleinschnitz C, Schmidt HH (2013) Neuroprotection after stroke by targeting NOX4 as a source of oxidative stress. *Antioxid Redox Signal* 18:1418-1427.
- Reisetter AC, Stebovanova LV, Baltrusaitis J, Powers L, Gupta A, Grassian VH, Monick MM (2011) Induction of inflammasome-dependent pyroptosis by carbon black nanoparticles. *J Biol Chem* 286:21844-21852.
- Schlunk F, Schulz E, Lauer A, Yigitkanli K, Pfeilschifter W, Steinmetz H, Lo EH, Foerch C (2015) Warfarin pretreatment reduces cell death and MMP-9 activity in experimental intracerebral hemorrhage. *Transl Stroke Res* 6:133-139.
- Schneider CA, Rasband WS, Eliceiri KW (2012) NIH Image to ImageJ: 25 years of image analysis. *Nat Methods* 9:671-675.
- Schürmann C, Rezende F, Kruse C, Yasar Y, Löwe O, Fork C, van de Sluis B, Bremer R, Weissmann N, Shah AM, Jo H, Brandes RP, Schröder K (2015) The NADPH oxidase Nox4 has anti-atherosclerotic functions. *Eur Heart J* 36:3447-3456.
- Shu XS, Zhu H, Huang X, Yang Y, Wang D, Zhang Y, Zhang W, Ying Y (2020) Loss of β -catenin via activated GSK3 β causes diabetic retinal neurodegeneration by instigating a vicious cycle of oxidative stress-driven mitochondrial impairment. *Aging (Albany NY)* 12:13437-13462.
- Takac I, Schröder K, Zhang L, Lardy B, Anilkumar N, Lambeth JD, Shah AM, Morel F, Brandes RP (2011) The E-loop is involved in hydrogen peroxide formation by the NADPH oxidase Nox4. *J Biol Chem* 286:13304-13313.
- Wilkinson-Berka JL, Rana I, Armani R, Agrotis A (2013) Reactive oxygen species, Nox and angiotensin II in angiogenesis: implications for retinopathy. *Clin Sci (Lond)* 124:597-615.
- Wu ST, Han JR, Yao N, Li YL, Zhang F, Shi Y, Shi FD, Li ZG (2022) Activation of P2X4 receptor exacerbates acute brain injury after intracerebral hemorrhage. *CNS Neurosci Ther* 28:1008-1018.
- Xie J, Hong E, Ding B, Jiang W, Zheng S, Xie Z, Tian D, Chen Y (2020) Inhibition of NOX4/ROS suppresses neuronal and blood-brain barrier injury by attenuating oxidative stress after intracerebral hemorrhage. *Front Cell Neurosci* 14:578060.
- Xie S, Jiang X, Doycheva DM, Shi H, Jin P, Gao L, Liu R, Xiao J, Hu X, Tang J, Zhang L, Zhang JH (2021) Activation of GPR39 with TC-G 1008 attenuates neuroinflammation via SIRT1/PGC-1 α /Nrf2 pathway post-neonatal hypoxic-ischemic injury in rats. *J Neuroinflammation* 18:226.
- Yan WT, Yang YD, Hu XM, Ning WY, Liao LS, Lu S, Zhao WJ, Zhang Q, Xiong K (2022) Do pyroptosis, apoptosis, and necroptosis (PANoptosis) exist in cerebral ischemia? Evidence from cell and rodent studies. *Neural Regen Res* 17:1761-1768.
- Zeng C, Duan F, Hu J, Luo B, Huang B, Lou X, Sun X, Li H, Zhang X, Yin S, Tan H (2020) NLRP3 inflammasome-mediated pyroptosis contributes to the pathogenesis of non-ischemic dilated cardiomyopathy. *Redox Biol* 34:101523.
- Zhang C, Jiang M, Wang WQ, Zhao SJ, Yin YX, Mi QJ, Yang MF, Song YQ, Sun BL, Zhang ZY (2020) Selective mGluR1 negative allosteric modulator reduces blood-brain barrier permeability and cerebral edema after experimental subarachnoid hemorrhage. *Transl Stroke Res* 11:799-811.
- Zhang W, Hu X, Shen Q, Xing D (2019) Mitochondria-specific drug release and reactive oxygen species burst induced by polyprodrug nanoreactors can enhance chemotherapy. *Nat Commun* 10:1704.
- Zhang Y, Wong HS (2021) Are mitochondria the main contributor of reactive oxygen species in cells? *J Exp Biol* 224:jeb221606.
- Zhi D, Cheng Q, Midgley AC, Zhang Q, Wei T, Li Y, Wang T, Ma T, Rafique M, Xia S, Cao Y, Li Y, Li J, Che Y, Zhu M, Wang K, Kong D (2022) Mechanically reinforced biotubes for arterial replacement and arteriovenous grafting inspired by architectural engineering. *Sci Adv* 8:eabl3888.
- Zhou M, Zhao X, Liao L, Deng Y, Liu M, Wang J, Xue X, Li Y (2022) Forsythiaside A regulates activation of hepatic stellate cells by inhibiting NOX4-dependent ROS. *Oxid Med Cell Longev* 2022:9938392.
- Zhu F, Zi L, Yang P, Wei Y, Zhong R, Wang Y, You C, Li Y, Tian M, Gu Z (2021) Efficient iron and ROS nanoscaevengers for brain protection after intracerebral hemorrhage. *ACS Appl Mater Interfaces* 13:9729-9738.

C-Editor: Zhao M; S-Editors: Yu J, Li CH; L-Editors: Wolf GW, Song LP; T-Editor: Jia Y